ACS APPLIED ENGINEERING MATERIALS

pubs.acs.org/acsaenm Article

Understanding the Structural–Chemical Evolution of Epitaxial NbN/Al_2O_3/NbN Trilayers with Varying NbN Thickness

Jith Sarker, Prachi Garg, Menglin Zhu, Christofer M. Rouleau, Jinwoo Hwang, Eric Osei-Agyemang, and Baishakhi Mazumder*

Cite This: *ACS Appl. Eng. Mater.* 2023, 1, 3227–3236 Read Online

ACCESS | Metrics & More | Article Recommendations | Supporting Information

ABSTRACT: Epitaxial NbN/Al_2O_3/NbN trilayer structures with NbN thicknesses of 50–200 nm were grown by pulsed laser deposition. Within each trilayer configuration, it was observed that the top NbN layers exhibited slightly reduced crystallinity compared to the bottom NbN layers due to the strain-induced effects caused by the lattice mismatch between NbN and Al_2O_3. Notably, the trilayer structures exhibited epitaxial growth with consistent in-plane rotational orientations in the NbN layers. Significant deviations in the stoichiometry of the NbN layers were detected, primarily stemming from N-deficient and O-rich regions. Moreover, the chemical non-uniformity within the NbN layers intensified as the layer thickness decreased. The lateral N/Nb distribution showed a complementary distribution with O/Nb, resulting from a higher tendency for NbO_x formation with lower NbN thicknesses. To gain a deeper understanding of the formation and impacts of local point defects, such as nitrogen vacancies and oxygen impurities, density functional theory (DFT) calculations were employed. The obtained defect formation energies suggest that O substitutional defects will prevail in an oxygen-rich environment over N vacancies. The investigation further explored the role of these defects in tuning the electronic states at the Fermi level.

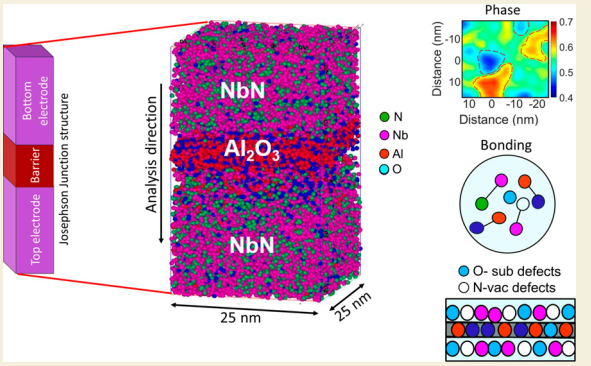

KEYWORDS: *Superconductors, Epitaxial growth, NbN/Al_2O_3/NbN trilayers, Crystallinity, Chemical inhomogeneity, Point defects*

I. INTRODUCTION

High-quality epitaxial NbN films exhibit exceptional quantum properties, such as high superconducting transition temperatures (T_c), increased critical current densities (J_c), and low residual resistivity ratios (RRRs).[1−5] Such enhanced superconducting characteristics hold great potential for the development of quantum devices, particularly Josephson junctions (JJs), in the field of quantum information and computation.[5−7] To further enhance the quantum properties of JJs, the adoption of epitaxial tunnel barriers, which feature fewer defect states compared to conventional amorphous tunnel barriers, is advised.[6,8−11] Previously demonstrated all-epitaxial NbN/AlN/NbN JJs have shown improved quantum properties, especially coherence time in qubits resulting from reduced defect densities.[12] This reduced defect density is attributed to their epitaxial nature with fewer crystal defects/disorders. However, one notable challenge with these JJs is the high piezoelectricity of AlN tunnel barriers, which contributes to enhanced qubit−phonon coupling, resulting in the reduction of the qubit relaxation time.[13] Therefore, there is a need for alternative tunnel barrier materials with low piezoelectric properties, such as Al_2O_3, to achieve reduced qubit−phonon coupling. Prior attempts to grow these NbN-based trilayer Josephson structures by employing high-density chemical vapor deposition (HDCVD), atomic layer deposition (ALD), and magnetron sputtering at very high substrate temperatures (T_S > 1000 °C) have been hindered by undesired chemical interdiffusions.[14,15] While a very low T_S (~350 °C) decreases the T_c to 13.8 K,[16] a relatively higher T_S introduces a larger grain size. It has been reported that such enhanced grain size improves the T_c; for instance, increasing the grain size from 15 to 35 nm results in an increase in the T_c from 12.6 to 16 K.[17] NbN films with larger grain sizes have fewer grain boundaries, yielding a lower defect density and less disorder. In this regard, pulsed laser deposition (PLD) emerges as a promising growth technique that is capable of achieving the desired lower T_S by employing high laser fluences.[15]

Despite the potential of all-epitaxial NbN/Al_2O_3/NbN trilayer structures grown by PLD for JJs, they have remained relatively unexplored. As far back as 1987, an epitaxial tunnel junction structure with NbN/Al_2O_3/NbN via ALD was

Received: September 14, 2023
Revised: November 17, 2023
Accepted: November 20, 2023
Published: December 12, 2023

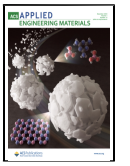

demonstrated by Talvacchio et al.[18] However, during this era, the practical applications of an all-epitaxial $NbN/Al_2O_3/NbN$ structure in future superconducting electronics were uncertain,[18] leading to a limited development of fully epitaxial trilayer Josephson structures for over two decades. Recently, it has been well established that epitaxial JJs offer a promising avenue for reduced two-level system (TLS) defects, contributing to enhanced quantum coherence in JJ devices.[6,8,10,11] Previously demonstrated epitaxial NbN/AlN/NbN qubits have offered superior coherence times (~500 ns), which were achieved due to the reduction in the TLS defect densities resulting from the epitaxial nature of the structures with less crystal disorder.[6,8] Motivated by these prior studies, here we adapted PLD to introduce novel all-epitaxial $NbN/Al_2O_3/NbN$ trilayer structures for future Josephson junction applications. Past investigations have revealed that microscopic material features, such as the stoichiometry, chemical heterogeneity,[19−21] formation of secondary phase,[22−24] and presence of impurities,[16,22−26] exert a profound impact on the structure−property relationship within NbN-based JJ structures. Notably, the prevalence of O contamination in NbN, which is attributed to the higher binding energy of Nb−O compared to that of Nb−N,[16] underscores the imperative need to gain insight into the structural chemistry of $NbN/Al_2O_3/NbN$ trilayers at the atomic scale. While previous studies have explored the electronic and superconducting properties of pristine NbN polymorphs through density functional theory (DFT) calculations,[27−30] there remains a need for a comprehensive understanding of how local defects in NbN films influence these properties. Consequently, it is crucial to elucidate the effect of the local structural chemistry of NbN films and their trilayer Josephson structures on the associated material properties, including the electronic density of states (DOS) and the phonon density of states (DOS).

In this work, we fabricated fully epitaxial $NbN/Al_2O_3/NbN$ JJ structures with NbN layers of varying thicknesses with PLD. The crystallinity and orientation of these trilayer structures were investigated by transmission electron microscopy (TEM). Atom probe tomography (APT) was employed to probe the atomic-scale structural chemistry and the impurity distributions within the bulk structure. To provide a deeper understanding of the structure−property relationship in this material, we conducted DFT calculations, complementing the experimental observations. DFT allowed us to theoretically analyze the formations and impacts of local point defects, such as N vacancies and O impurities, which were challenging to ascertain through the correlative TEM and APT analyses. Furthermore, our investigation delved into the role of these local point defects in tuning the properties of the $Al_2O_3(0001)/NbN(111)$ interface, particularly their influence on the electronic DOS at the Fermi level (E_F).

II. EXPERIMENTS AND METHODS

Three $NbN/Al_2O_3/NbN$ trilayer structures with NbN thicknesses of 50 nm (sample I), 100 nm (sample II), and 200 nm (sample III) were grown by a KrF excimer laser (λ = 248 nm, $\tau_{fwhm} \leq$ 25 ns) PLD system on c-plane sapphire (0001) substrates (5 mm × 5 mm). The laser beam was oriented at 45° with respect to the target surface. A Nb target with N flow was used for the NbN depositions, while an Al target with O flow was implemented for the Al_2O_3 depositions. The gas pressure was maintained at 50 mTorr with a gas flow of 10 sccm (standard cubic centimeter per minute). An aperture setting of 12 nm × 12 nm, a laser energy of ~100 mJ, a laser voltage of 20 kV, and a spot size of 1.4 × 1.5 nm^2 was used for each case. No laser attenuation (i.e, 100% transmission) was set during the growth. For the NbN layers, the incident laser fluence was set at ~5 J/cm^2, and the temperature was maintained at 600−610 °C. Then 5000, 10 000, and 20 000 laser shots were applied at a laser pulse frequency (LPF) of 10 Hz for samples I, II, and III, respectively. The deposited NbN layers were ~50, 100, and 200 nm thick for samples I, II, and III, respectively. After the first NbN layers (bottom electrodes) were deposited, the thin dielectric Al_2O_3 layers were deposited over the NbN layers. For Al_2O_3 deposition, the laser fluence was set to 2.5 J/cm^2, and the chamber temperature was raised to 825−850 °C. All of the other growth parameters remained unchanged. Then, 300 laser shots at an LPF of 10 Hz were applied, resulting in Al_2O_3 layers with a thickness of ~3 nm in each case. After the thin Al_2O_3 dielectric layers were deposited, the top NbN electrodes were deposited. For this, the laser fluence was changed to 5 J/cm^2, and the chamber temperature was reduced to 600−625 °C with all of the other parameters remaining the same. Then, similar to the growth of the bottom NbN electrode layers, 5000, 10 000, and 20 000 laser shots were introduced at an LPF of 10 Hz for samples I, II, and III, respectively. This resulted in top NbN electrodes having thicknesses of 50, 100, and 200 nm, respectively, grown over the thin Al_2O_3 dielectric layers. During the growth of each layer, streaky reflection high-energy electron diffraction (RHEED) patterns were observed, which confirm that the growths were epitaxial. A Thermo Fisher Scientific Titan scanning transmission electron microscope (STEM) operating at 300 kV was used to acquire high-angle annular dark-field (HAADF) high-resolution (HR) STEM images and nanodiffraction images.

The needle-shaped APT specimens were prepared by using a Thermo Fisher Nova 200 dual-beam focused ion beam (FIB)/scanning electron microscope (SEM). The sharp APT needles were prepared by following standard site-specific lift-out and annular milling methods.[31,32] The APT data acquisition was performed on a CAMECA LEAP 4000X HR instrument in laser mode (laser wavelength (λ) = 355 nm) with a laser energy of 100−125 pJ, a specimen temperature of 50 K, a pulse repetition rate of 200 kHz, and a 0.5% detection rate. The APT data analysis was conducted using CAMECA's Integrated Visualization and Analysis Software (IVAS 3.8). Details about the APT instrumentation and reconstruction algorithms are reported elsewhere.[33,34]

First-principles calculations were conducted using a DFT approach by employing the Vienna ab initio simulation package (VASP), which serves as a computational tool for electronic structure analysis.[35] To approximate the exchange-correlation energy of electrons in the material, the generalized gradient approximation (GGA)[36] method, specifically the Perdew−Burke−Ernzerhof (PBE) functional, was employed.[36] Additionally, assessments of the electronic structure and properties were carried out through the solution of the Kohn−Sham equations alongside the utilization of the projector augmented wave (PAW) method. These calculations considered the spin states of the electrons, a fundamental quantum property, by incorporating spin polarization. Furthermore, a Gaussian smearing technique was applied uniformly with a smearing width (σ) of 0.05 eV for all of the computational processes. The calculations focused on the δ-NbN crystal in the cubic $Fm3m$ phase. The optimization process began with the NbN(111) surface, which was used in building the interfacial structure. Meanwhile, the $Al_2O_3(0001)$ surface served as the substrate, and its lattice parameter was used as the base for the interfacial structure. This approach allowed for the consideration of different lattice parameters at the surface and base. During the interfacial optimization, four layers of both Al_2O_3 and NbN closer to the interface were relaxed, while the remaining layers were fixed to mimic the bulk properties. To attain a ground state convergence, the evaluation of the total energy relied on a plane-wave basis set with an energy cutoff of 500 eV, and a 4 × 4 × 2 Γ-centered Monkhorst−Pack k-point grid was employed. To accurately calculation the total and partial electronic DOS, a finer 6 × 6 × 2 k-point grid was utilized. Lattice relaxation was performed using the force-based conjugate gradient approach[37] with an energy convergence tolerance of 10^{-6} eV and a minimum force/atom tolerance of 0.001 eV/Å.

https://doi.org/10.1021/acsaenm.3c00555
ACS Appl. Eng. Mater. 2023, 1, 3227−3236

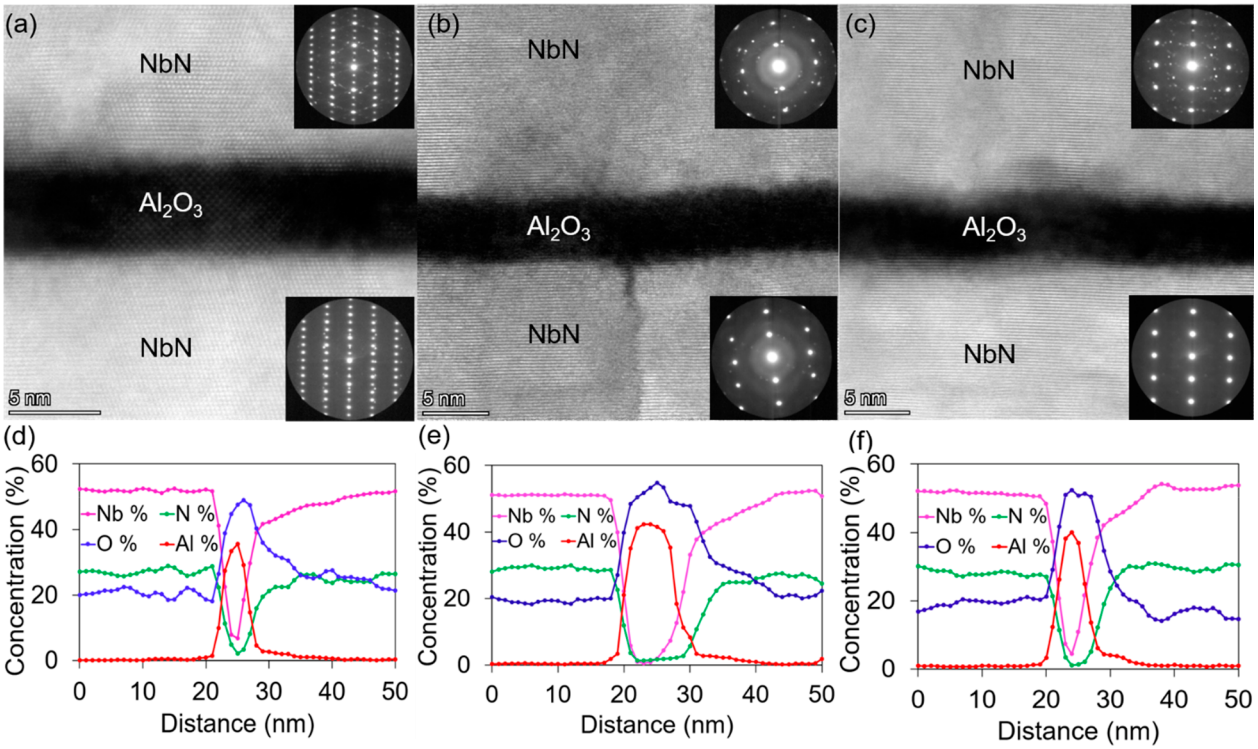

Figure 1. High-resolution HAADF STEM imaging of epitaxially grown NbN/Al_2O_3/NbN trilayer structures having (a) 50, (b) 100, and (c) 200 nm thick NbN layers grown on (0001)−Al_2O_3 substrates, revealing the diffusive nature of the NbN/Al_2O_3 interfaces. The SAED patterns for the top and bottom NbN layers are shown in the insets of (a)−(c). The local composition profiles across the interfacial region of the (b) 50, (d) 100, and (f) 200 nm thick samples show that the bottom interfaces are diffusive in nature (specially, O diffusion) compared to the top counterparts.

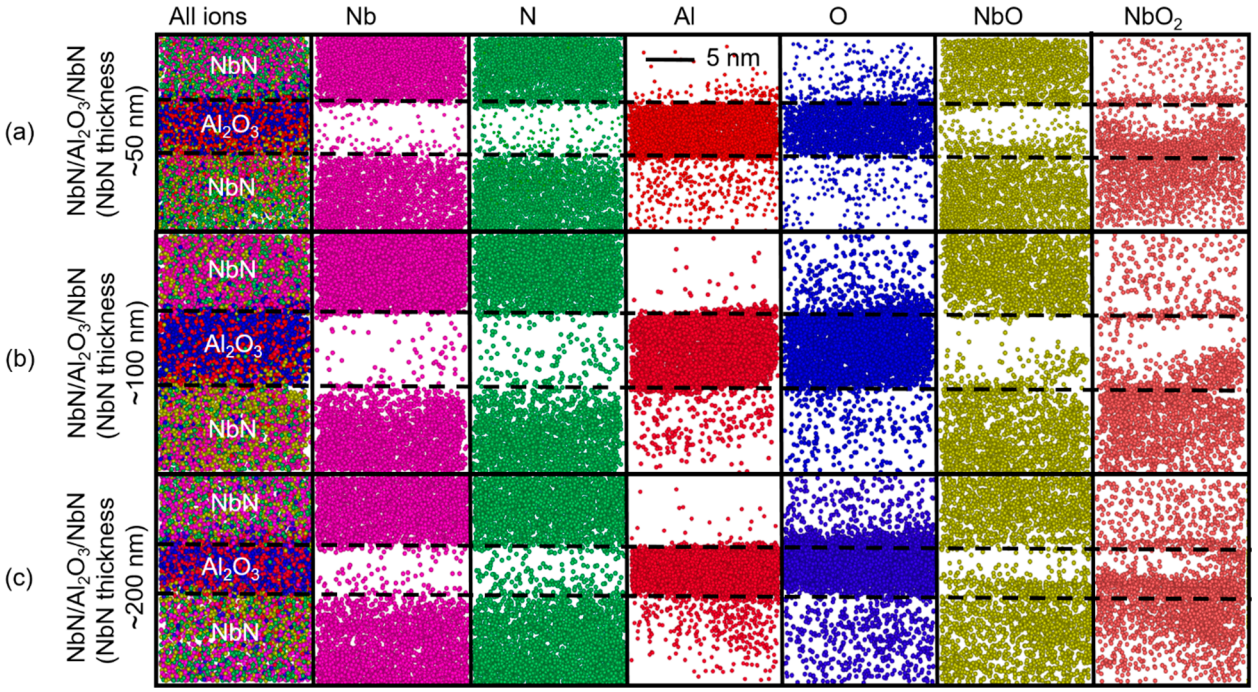

Figure 2. 3D atomic distributions of the NbN/Al_2O_3/NbN trilayer structures having (a) 50, (b) 100, and (c) 200 nm thicknesses across the interfaces, showing the distribution of (from left to right) all ions, Nb, N, Al, O, NbO, and NbO_2.

III. RESULTS AND DISCUSSION

The crystallinity of the PLD-grown NbN/Al_2O_3/NbN trilayer structures with 50, 100, and 200 nm thick NbN layers was observed by high-resolution HAADF STEM imaging, as depicted in panels a−c of Figure 1, respectively. The NbN and Al_2O_3 dielectric layers can be readily distinguished based on their contrast variation. The nanodiffraction patterns for each NbN layer within all three trilayer structures are presented in the insets of Figure 1a−c. An analysis of these nanodiffraction patterns reveals that the top NbN layers exhibit

https://doi.org/10.1021/acsaenm.3c00555
ACS Appl. Eng. Mater. 2023, 1, 3227−3236

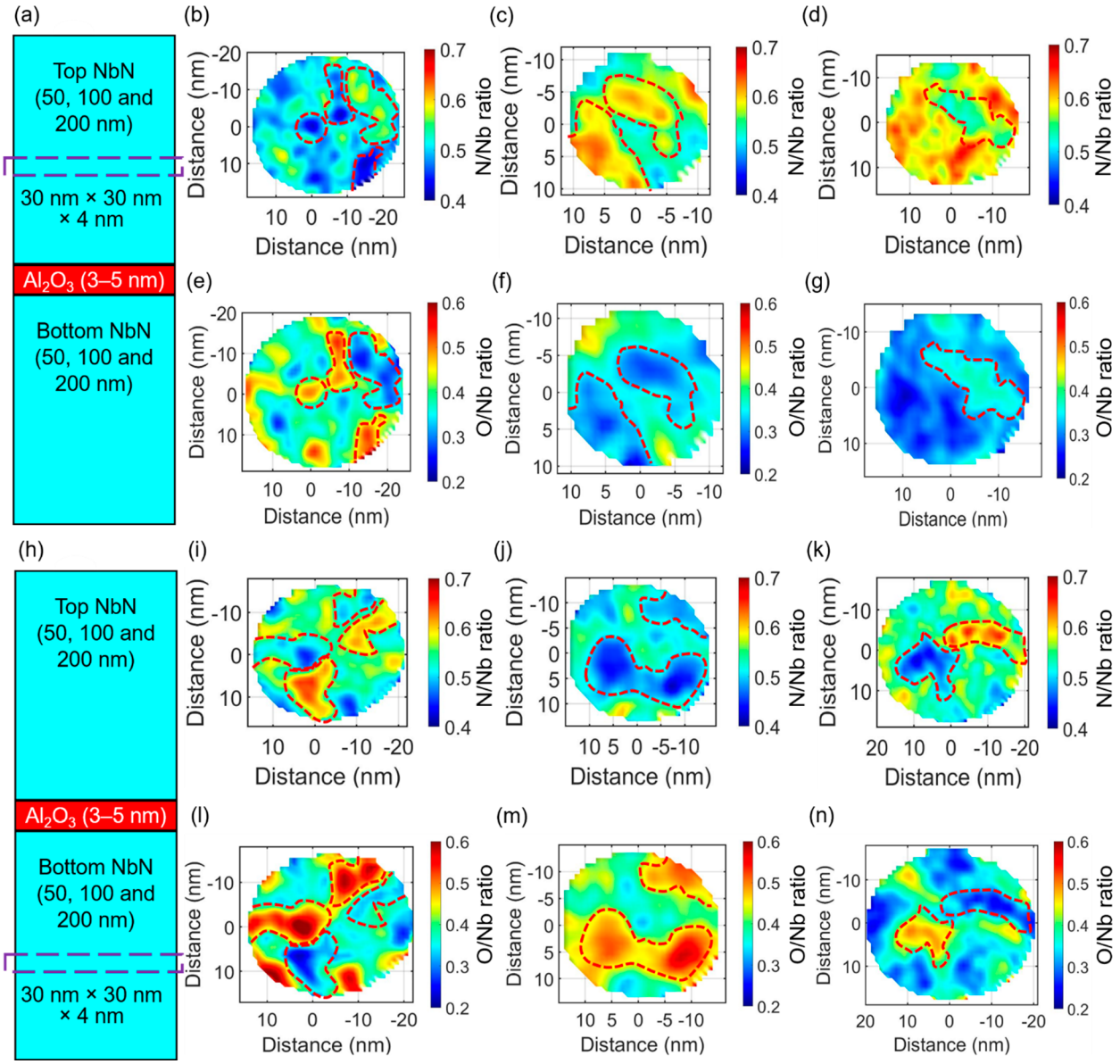

Figure 3. (a) A schematic showing the dimensions of the NbN/Al_2O_3/NbN trilayer structures with different NbN thicknesses. A volume of 30 × 30 × 4 nm^3 was extracted from the bulk of the top NbN layers for local chemical analysis. The lateral distribution of the N/Nb profiles for the (b) 50, (c) 100, and (d) 200 nm thick NbN films are complemented by O impurities, as shown by the lateral O/Nb profiles in (e)−(g), respectively. The complementary N and O distributions are marked by the dotted regions, which indicate the presence of Nb oxide-based secondary phases within the NbN layers. (h) A schematic showing the dimension of the NbN/Al_2O_3/NbN trilayer structures with different NbN thicknesses. A volume of 30 × 30 × 5 nm^3 was extracted from the bulk of the bottom NbN layers for local chemical analysis. The lateral distribution of the N/Nb profiles for the (i) 50, (j) 100, and (k) 200 nm thick NbN films are complemented by O impurities, as shown by the lateral O/Nb profiles in (l)−(n), respectively. The complementary N and O distributions are marked by the dotted regions, indicating the presence of Nb oxide-based secondary phases within the NbN layers.

slightly reduced crystallinity compared to the bottom NbN layers, indicated by the presence of additional spots in the nanodiffraction patterns for the top NbN layers that are otherwise absent in the bottom NbN layers. This difference can be attributed to the lattice mismatch between the Al_2O_3 dielectric layers over which the NbN layers are grown.[38] The Al_2O_3 layers show reduced crystallinity, with some nanocrystalline regions identified in Figure 1a−c. The HAADF STEM imaging further confirms the epitaxial growth of the NbN layers with in-plane rotational crystal orientations, which are of significant importance in determining their superconducting and tunneling properties.[39] Additionally, the quantum properties of NbN/Al_2O_3/NbN trilayer structures can be influenced by the chemical diffusions at the NbN/Al_2O_3 interfaces. Via STEM imaging, visibly diffused NbN/Al_2O_3 and Al_2O_3/NbN interfaces were observed for all three structures. To substantiate these visual interfacial characteristics at the atomic scale, a technique with superior spatial resolution and chemical sensitivity is required.[40−42] In this regard, APT was employed to investigate the atomic-scale chemical interdiffusions across both the top and bottom interfaces in all three structures, as illustrated in Figure 1d−f. The composition profiles of Nb, N, Al, and O across the NbN/Al_2O_3 interfaces are shown in panels d−f of Figure 1 for the structures with

https://doi.org/10.1021/acsaenm.3c00555
ACS Appl. Eng. Mater. 2023, 1, 3227−3236

NbN layer thicknesses of 50, 100, and 200 nm, respectively. While the top interfaces exhibit atomic-level abruptness in all cases, all three structures exhibit substantial oxygen diffusion from Al_2O_3 into the NbN layers at the bottom interfaces. Such diffusive interfaces are likely to result in higher interfacial barrier heights, potentially leading to reduced tunneling properties in these trilayer structures.[43]

Investigating the underlying causes of the observed differences in the NbN layer crystallinity, particularly in relation to the varying NbN layer thickness, was of the utmost significance. To achieve this, APT was employed due to its exceptional chemical sensitivity and high spatial resolution to probe the atomic-scale structural chemistry of the NbN layers. Panels a−c of Figure 2 illustrate the three-dimensional (3D) atomic distributions of Nb, N, Al, and O across the interfacial regions for the $NbN/Al_2O_3/NbN$ trilayer structures with NbN layer thicknesses of 50, 100, and 200 nm, respectively. A noteworthy observation is the prevalence of secondary NbO_x formations in the NbN layers grown over the oxide substrates, which are attributed to the pronounced affinity of Nb for oxygen over nitrogen.[16] The APT data also highlight the distinct peaks in the mass spectra corresponding to the atomic distributions of NbO_x (including NbO and NbO_2). While the 3D atomic distributions of Nb and N are as expected, Al is observed to diffuse in the bottom NbN layers. The reason for Al diffusion being limited to only the bottom NbN layers remains unknown and warrants further studies. A considerable concentration of O atoms is evident within the bulk regions of the top and bottom NbN layers for the three structures. Although it is plausible that these oxygen atoms diffused from the Al_2O_3 dielectric layer due to the high affinity of Nb to O compared to N,[16,44] the presence of undesired O may also result from its incorporation during the growth process or surface exposure of the structures. The presence of this O impurity would drastically affect the local structural chemistry of the NbN layers by creating point defects and forming a secondary oxide phase. In this study, NbO and NbO_2 are detected in the APT mass spectra, as shown in Figures S1−S3, and their corresponding 3D distributions are shown in Figure 2 for all of the $NbN/Al_2O_3/NbN$ trilayer structures.

The superconducting properties of NbN layers and, consequently, the overall trilayer structures are significantly influenced by in-plane chemical homogeneity (N:Nb stoichiometry) and the formation of NbO_x compounds.[24] To investigate the lateral chemical variations within the bulk region of both the top and bottom NbN layers across all three structures, we conducted an analysis. The schematic in Figure 3a depicts the $NbN/Al_2O_3/NbN$ trilayer structures with NbN thicknesses of 50, 100, or 200 nm. From the bulk region of the top NbN layers, volumes of $30 \times 30 \times 4$ nm^3 were extracted, as indicated by the purple dotted box, to probe the in-plane chemical distributions. The N/Nb distributions associated with the 50, 100, and 200 nm thick top NbN layers are shown in Figure 3b−d, respectively. The 50 nm thick NbN layer exhibits a more inhomogeneous N/Nb distribution (ranging from 0.4 to 0.6) compared to the N/Nb inhomogeneities of 0.55−0.65 observed in the thicker NbN layers with thicknesses of 100 and 200 nm, revealing the presence of both N-deficient and N-rich zones. The higher N/Nb inhomogeneity observed with a lower NbN thickness is attributed to the strain induced by the lattice mismatch between the NbN films and the Al_2O_3 dielectric layers.[24,38] Figure 3e−g shows the O/Nb distributions within the same extracted volumes used for the N/Nb distributions of the 50, 100, and 200 nm thick top NbN layers. In all three cases, the O/Nb lateral distributions are complementary to the respective N/Nb distributions. As the NbN thickness decreases, O/Nb becomes more inhomogeneous (O/Nb ∼ 0.25−0.55), as shown in Figure 3e for the 50 nm thick NbN layer. In contrast, O/Nb ratios of 0.3−0.4 are observed for the 100 and 200 nm thick NbN layers (panels f and g of Figure 3, respectively). These non-uniform O/Nb ratios result from the presence of both O-deficient and O-rich regions, which corresponding exactly to the N-rich and N-deficient regions. The observed chemical inhomogeneity in the top NbN layers with varying thicknesses was further confirmed via statistical frequency distribution analysis (FDA) using a bin size of 200 atoms, as shown in Figure S4a−g. Similar in-plane N/Nb and O/Nb distributions, influenced by the varying NbN thickness, were also observed in the bottom NbN layers, as illustrated in Figure 3h−n. The volumes extracted from the bottom NbN layers are shown by the purple dotted box in the schematic in Figure 3h. Figure 3i−k shows the lateral N/Nb distributions in the bottom NbN layers with thicknesses of 50, 100, and 200 nm, respectively, while Figure 3l−n depicts the corresponding O/Nb distributions. As observed in the top NbN layers, reducing the thickness of the bottom NbN layer resulted in increased inhomogeneity, accompanied by corresponding lateral O/Nb distributions similar to those found in N/Nb. The higher N/Nb inhomogeneity that was observed by reducing the NbN thickness is due to substrate strain effects.[24,38] The complementary O/Nb distributions with N/Nb in both the top and bottom NbN layers are mainly attributed to the formation of secondary NbO_x phases (as marked by the dotted regions for both the top and bottom NbN layers with thicknesses of 50, 100, and 200 nm) within the NbN layers.[24] The corresponding FDA plots are reported in Figure S4h−n, which confirm the chemical inhomogeneity increases as the layer thickness decreases.

Apart from the strain induced by lattice mismatching, the observed N/Nb inhomogeneity might also be associated with N:Nb stoichiometric deviations introduced by the presence of a considerable amount of N vacancies, which is typical in NbN films.[19,20,45,46] Alongside the formation of secondary NbO_x phases, O atoms that are incorporated within NbN films as local substitutional or interstitial point defects typically play a pivotal role in tuning the superconducting properties of NbN layers and, hence, the quantum behavior of $NbN/Al_2O_3/NbN$ trilayers.[16,24] Because of the detection limit of correlative TEM and APT, it is extremely difficult to probe the formation of local point defects, such as N vacancies and substitutional/interstitial O impurities, and their effects on the local structure of NbN films. To address this information void, a theoretical investigation using first-principles DFT calculations was adapted in the next part of this work to provide a complete understanding of the effect of local point defects on the NbN crystal structure and its properties.

Crystallographic imperfections in these materials are known to exert a significant influence on the material properties. For instance, a substantial presence of nitrogen vacancies in the NbN phase, along with the formation of oxygen substitutional states, is due to the Al_2O_3 interface.[19] Hence, first-principles calculations were employed to investigate these N vacancies and O substitutional states in the trilayer structure while accounting for the interfacial properties. NbN possesses a cubic crystal structure, belonging to space group *Fm*3*m*, with an even distribution of 50% niobium and 50% nitrogen. The

https://doi.org/10.1021/acsaenm.3c00555
ACS Appl. Eng. Mater. 2023, 1, 3227−3236

cubic phase of NbN predominantly features the (111) surface, making it our primary choice for constructing the Al_2O_3/NbN interface.[47] We built this interface with Al_2O_3(0001) and NbN(111) surfaces by constraining the NbN structure to the lattice of the Al_2O_3(0001) surface. The lattice vectors for the final interfacial model as well as the Al_2O_3(0001) surface had the following parameters: $a = b = 1.3947$ nm, $\alpha = \beta = 90°$, and $\gamma = 120°$. The corresponding parameters for the NbN(111) surface used in building the interface were $a = b = 1.2594$ nm, $\alpha = \beta = 90°$, and $\gamma = 120°$. This yielded a lattice mismatch of approximately 10%.

The structure obtained through DFT calculations revealed a noticeable reduction in the crystallinity at the interface, as illustrated in Figure 4. This shift in the crystalline structure was

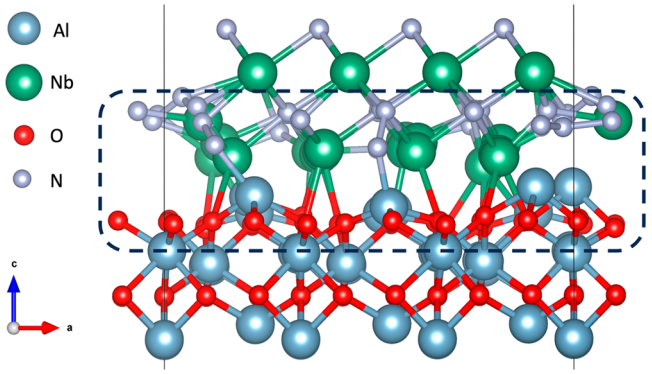

Figure 4. Interfacial region of the Al_2O_3(0001)/NbN(111) structure. The dotted box shows the reduced crystallinity at the interfacial region. This effect is more pronounced in the NbN region.

visually evident through the distinct arrangement of the interfacial atoms and bonds when compared to the unmarked region, which depicted bulk-like features. Additionally, the diminished crystallinity at the interface became apparent when analyzing the interfacial bond distances compared those in the bulk structure. For instance, in the bulk regions, Al−O bond distances were measured to be 0.1923 and 0.1818 nm, whereas at the interface, these distances were calculated to be 0.1764, 0.1736, and 0.1948 nm. Similarly, in the bulk region, Nb−N bond distances were 0.2226 nm, whereas at the interface, they were measured to be 0.2051, 0.2171, and 0.2140 nm. The Nb−O bond distances at the interface were 0.2334 and 0.2019 nm, while the Al−N bond distances at the interface were 0.1940 and 0.1850 nm. The reduced crystallinity was more prominent in the NbN region compared to the Al_2O_3 region at the interface, corroborating the experimental findings. Significantly, the lattice constant for the interfacial structure was constrained to the optimized value for Al_2O_3 in the (0001) direction. This constraint ensured that the NbN film aligned with the Al_2O_3 lattice, which provided further insight into why the decrease in crystallinity was more prominent within the NbN region of the interface.

The presence of N vacancies in the trilayer structure and the presence of O atoms diffusing from Al_2O_3 to the NbN region could affect the superconducting properties of Nb. To investigate these defects in the NbN region of the trilayer interfacial structure, we estimated the defect formation energy (DFE) by using the following equations:[48]

$$\Delta E_{\text{N vacancy}} = E_{\text{NbN}_{1-x}} - E_{\text{NbN}} + x\mu_{\text{N}}$$

$$\Delta E_{\text{O substitute}} = E_{\text{NbN}_{1-x}\text{O}_x} - E_{\text{NbN}} + x\mu_{\text{N}} - x\mu_{\text{O}}$$

Here, E_{NbN}, $E_{\text{NbN}_{1-x}}$, and $E_{\text{NbN}_{1-x}\text{O}_x}$ are the total ground-state DFT energies of the pristine, N-vacant, and O-substituted NbN relaxed interfacial structures, respectively. x denotes the number of N vacancies formed or the number of O atoms that were substituted for the N vacancies. μ_{N} and μ_{O} denote the chemical potentials of N and O, respectively, which were approximated as the ground-state DFT energies of N and O in their standard states. These were computed to be equal to half of the total energies of single gaseous N_2 and O_2 molecules. O_2 gas was used as the reference state for μ_{O}, while N_2 gas was used as the reference state for μ_{N}, as N_2 gas flow was used to prepare the thin films. The considered defect concentrations for both the N vacancies and O substitutions were 2.44%, 4.88%, and 7.32%. Figure 5 shows the DFEs of the N vacancies and O substitutional defects at various defect concentrations for the NbN/Al_2O_3/NbN trilayer interfacial structure.

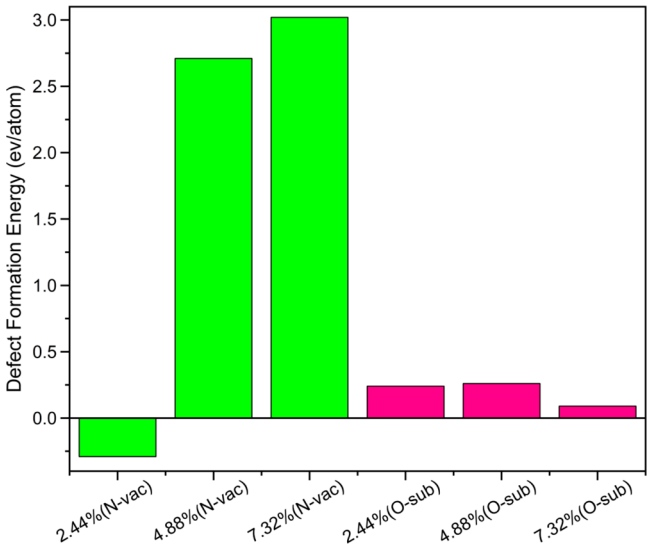

Figure 5. Defect formation energies of varying concentrations of N vacancies and O substitutional defects in the Al_2O_3(0001)/NbN(111) interfacial structure.

Assessing the defect formation energy is a valuable indicator of defect stability within the crystal lattice. For example, lower values of defect formation energy signify that the creation of a defect is energetically favorable because it reduces the total energy of the crystal lattice. Our observations revealed that a negative DFE was linked to low N vacancy concentrations, particularly when these concentrations were <2.5%. However, as the number of introduced N vacancies increased, the DFE increased, indicating a decrease in the defect stability. In contrast, the substitution of O atoms was energetically unfavorable at lower O concentrations. As we introduced O atoms to replace N atoms within the NbN layers from an O reservoir, we observed that these defects became progressively more stable with an increase in the concentration of the substituted O atoms. As depicted in Figure 5, the DFE values for O substitution converge around 0, indicating that O substitutions are more energetically preferrable than N vacancies to maintain the overall stability in the NbN/Al2O3/NbN trilayer structure. This finding is in agreement

https://doi.org/10.1021/acsaenm.3c00555
ACS Appl. Eng. Mater. 2023, 1, 3227−3236

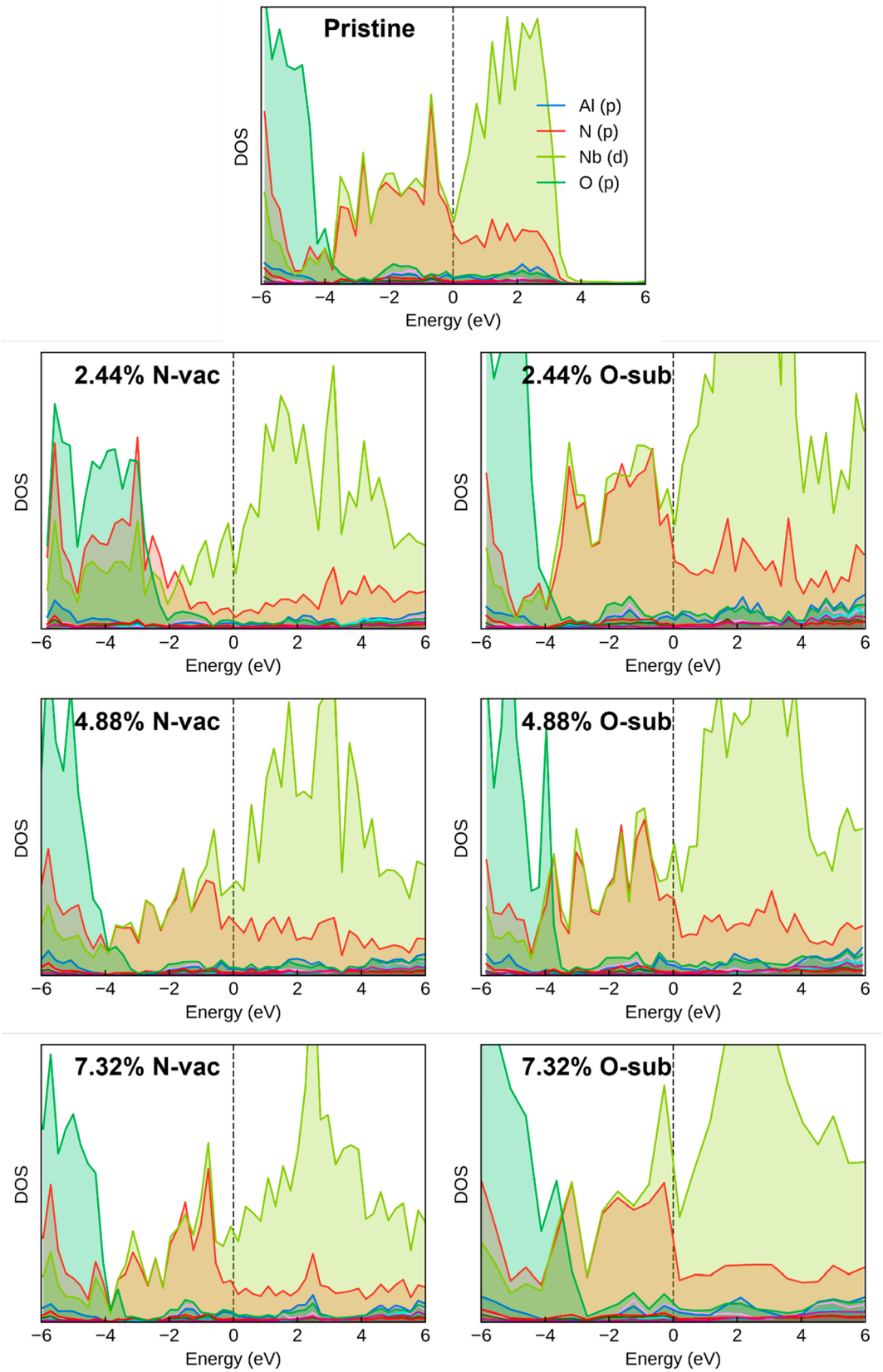

Figure 6. Effect of N vacancies and O substitutional defects on the electronic density of states of the $Al_2O_3(0001)/NbN(111)$ interface. The plots highlight the changes of the DOS at the Fermi level (marked by the dashed vertical line). The labels for all defect concentrations are the same as those shown for the pristine structure: blue, contributions from Al p orbitals; red, N p orbitals; light green, Nb d orbitals; and dark green, O p orbitals.

https://doi.org/10.1021/acsaenm.3c00555
ACS Appl. Eng. Mater. 2023, 1, 3227−3236

with the experimental observations of the O atoms efficiently incorporating themselves into the NbN region of the trilayer structure.

Understanding the electronic density of states (the number of available energy states) at the Fermi level is crucial for determining how materials conduct electricity and exhibit superconducting behavior. The Al_2O_3/NbN interface reflects the characteristics of NbN, which has a nonzero electronic density of states $N(E_f)$ at the Fermi level and behaves like a metal.[28] The electronic DOS with contributions from the Nb, N, and O orbitals are shown in Figure 6. In the pristine structure, Figure 6 shows predominant contributions from the Nb d and N p orbitals at the Fermi level. Nb d states are prevalent at the conduction band minimum (CBM), while both Nb d and N p states contribute equally at the valence band maximum (VBM). The formation of various defect structures highlights significant contributions from both the Nb d and N p orbitals around the Fermi level. When N atoms are removed from the lattice (defect structures), the contributions from the N p states at the Fermi level decrease drastically compared to the pristine structure, while those from the Nb d states increase significantly. Furthermore, substituting N atoms with O atoms in the lattice (O-sub defects) results in a significant increase in Nb d states at the Fermi level, while N p states shift to higher energies toward the conduction band in comparison to the pristine structure. For O substitutional defects, major contributions from the O 2p states appear in the valence band region around −4 eV, although higher O concentrations push the O 2p states toward the Fermi level. Both the VBM and the CBM are dominated by Nb d and N p states. As a result, it is suggested that optimizing the levels of both Nb and N within the trilayer structure could potentially enhance the superconducting properties of the material. This hypothesis could be further substantiated through additional analysis of the trilayer's superconducting characteristics in future investigations.

The variation of $N(E_f)$ with the defect concentration is shown in Figure 7. Notably, the pristine $Al_2O_3(0001)$/NbN(111) interface exhibits the lowest $N(E_f)$ value in comparison with the interfaces with introduced defect states. Both the presence of N vacancies and O substitutional defects result in a similar pattern of increasing $N(E_f)$. As the concentration of the N vacancies and O substitutional defects rises, $N(E_f)$ also increases. However, Figure 5 shows that high N vacancy concentrations are unstable due to the high defect formation energy. Therefore, lower concentrations of N vacancies or higher concentrations of O substitutional defects (stable defects) will generate higher density of states at the Fermi level and subsequently lead to increased superconductivity. A deeper comprehension of electron−phonon coupling is crucial for understanding the superconducting temperature of this material. Higher states at the Fermi level intensify electron−phonon coupling, and the presence of O substitutional defects and a lower concentration of N vacancies enhances the coupling. This increased electron−phonon coupling may potentially lead to a lower T_c for superconductivity.

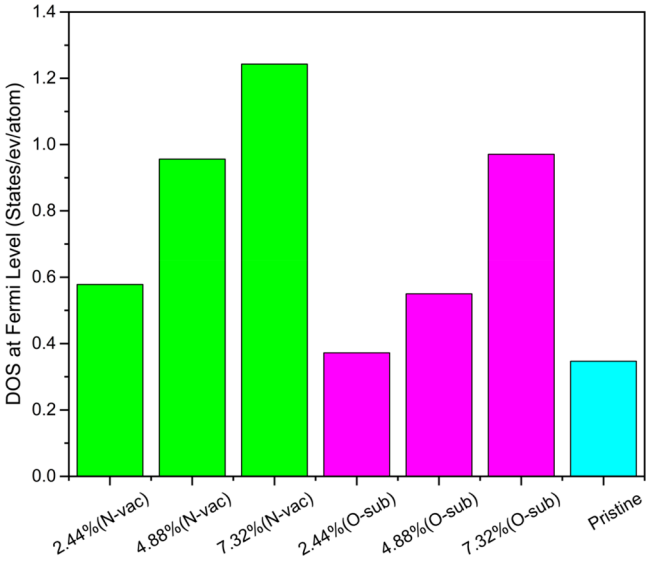

Figure 7. Electronic density of states at the Fermi level of pristine NbN and $Al_2O_3(0001)$/NbN(111) with N vacancies and O substitutional impurities.

It is evident from the DOS plots that the introduction of O atoms into the structure shifts the O 2p bands toward the Fermi level. This shift contributes to the states at the Fermi level, eventually increasing the electron−phonon coupling constant. Thus, the higher the oxygen content, the greater the $N(E_f)$ and the stronger the electron−phonon coupling.[49]

Because of the importance of the strength of the electron−phonon coupling constant, future analysis will be dedicated to the phonon structure and density of states as well as the estimation of the values of the electron phonon coupling constant for the pristine and defect-induced interfacial structures.

IV. CONCLUSION

Epitaxial NbN/Al_2O_3/NbN trilayer JJ structures with NbN thicknesses of 50, 100, and 200 nm were grown by pulse laser deposition. These trilayers were epitaxial, as confirmed by high-resolution STEM imaging, revealing in-plane rotational orientations within the NbN layers. In these epitaxial arrangements, an evident trend emerged: the top NbN layers exhibited slightly reduced crystal quality compared to the bottom NbN layers due to the strain induced by the lattice mismatch between NbN and Al_2O_3. Furthermore, our investigation delved into the atomic-scale structural chemistry of these NbN/Al_2O_3/NbN trilayers using APT. This revealed that the inhomogeneity (in-plane N/Nb distribution) within the NbN layers increased as the layer thickness decreased, showing significant stoichiometric variations marked by N-deficient and O-rich regions. The in-plane N/Nb distribution exhibited a complementary pattern with that of O/Nb, indicating a higher tendency of NbO_x formation within the NbN layers as the film thickness decreased. The role of local point defects, including N vacancies and O impurities, were then explored using DFT calculations. The calculated defect formation energies using DFT suggested that, in an oxygen-rich environment, the prevalence of O substitutional defects would outweigh that of N vacancies. Crucially, our analysis of the electronic density of states at the Fermi level uncovered that the $Al_2O_3(0001)$/NbN(111) structure with O substitutional defects and a low amount of N vacancies exhibited a higher electronic DOS than the pristine $Al_2O_3(0001)$/NbN(111) structure. This enables stronger electron−phonon coupling in the $Al_2O_3(0001)$/NbN(111) structure with O substitutional defects, ultimately leading to a higher critical temperature (T_c) than that observed in the pristine structure

https://doi.org/10.1021/acsaenm.3c00555
ACS Appl. Eng. Mater. 2023, 1, 3227−3236

or structures with N vacancies. The atomic-scale understanding provided in this work will offer valuable guidance for the development of NbN-based Josephson junction structures for future high-performance quantum computers.

■ ASSOCIATED CONTENT

Supporting Information

The Supporting Information is available free of charge at https://pubs.acs.org/doi/10.1021/acsaenm.3c00555.

APT mass spectra and frequency distribution analysis of the epitaxial NbN/Al_2O_3/NbN trilayer structures having 50, 100, and 200 nm thick NbN layers (PDF)

■ AUTHOR INFORMATION

Corresponding Author

Baishakhi Mazumder − *Department of Materials Design and Innovation, University at Buffalo, Buffalo, New York 14260, United States;* orcid.org/0000-0003-1748-5297; Email: baishakh@buffalo.edu

Authors

Jith Sarker − *Department of Materials Design and Innovation, University at Buffalo, Buffalo, New York 14260, United States*

Prachi Garg − *Department of Materials Design and Innovation, University at Buffalo, Buffalo, New York 14260, United States*

Menglin Zhu − *Department of Materials Science and Engineering, Ohio State University, Columbus, Ohio 43212, United States*

Christofer M. Rouleau − *Center for Nanophase Materials Sciences, Oak Ridge National Laboratory, Oak Ridge, Tennessee 37830, United States*

Jinwoo Hwang − *Department of Materials Science and Engineering, Ohio State University, Columbus, Ohio 43212, United States*

Eric Osei-Agyemang − *Department of Materials Design and Innovation, University at Buffalo, Buffalo, New York 14260, United States;* orcid.org/0000-0002-9805-9021

Complete contact information is available at: https://pubs.acs.org/10.1021/acsaenm.3c00555

Author Contributions

J.S. performed the material growth experiments, APT data reconstruction and analysis, and manuscript writing. P.G. performed data analysis and manuscript writing. M.Z. performed the STEM experiments and analysis. E.O.-A. conducted the DFT calculations. C.M.R. performed the growth of the trilayer structures. J.H. supervised the STEM experiments. B.M. conceptualized the project, supervised the experiments, and performed data analysis, manuscript writing, reviewing, and editing.

Funding

J.S., P.G., and B.M. would like to acknowledge the support from the National Science Foundation (NSF) under DMR (Grants 2114595 and 2145091). M.Z. and J.H. acknowledge the support from NSF under DMR-2011876.

Notes

This manuscript has been authored by UT-Battelle, LLC under Contract No. DE-AC05-00OR22725 with the U.S. Department of Energy. The United States Government retains and the publisher, by accepting the article for publication, acknowledges that the United States Government retains a non-exclusive, paid-up, irrevocable, world-wide license to publish or reproduce the published form of this manuscript, or allow others to do so, for United States Government purposes. The Department of Energy will provide public access to these results of federally sponsored research in accordance with the DOE Public Access Plan (http://energy.gov/downloads/doe-public-access-plan).

The authors declare no competing financial interest.

■ ACKNOWLEDGMENTS

Epitaxial growth of the trilayer structures and the APT experiments were conducted in the Center for Nanophase Materials Sciences (CNMS), which is a U.S. Department of Energy, Office of Science User Facility at Oak Ridge National Laboratory. The authors thank Dr. Jonathan Poplawsky and Mr. James Burns for the APT specimen preparations and for conducting the APT experiments.

■ REFERENCES

(1) Kaul, A. B.; Sands, T. D.; Duzer, T. V. High-Tc superconducting NbN films with low particulate density grown at 25 °C using pulsed laser deposition. *J. Mater. Res.* **2001**, *16* (5), 1223−1226.

(2) Bacon, D. D.; English, A. T.; Nakahara, S.; Peters, F. G.; Schreiber, H.; Sinclair, W. R.; van Dover, R. B. Properties of NbN thin films deposited on ambient temperature substrates. *J. Appl. Phys.* **1983**, *54* (11), 6509−6516.

(3) Makise, K.; Odou, T.; Ezaki, S.; Asano, T.; Shinozaki, B. Superconductor-insulator transition in two-dimensional NbN/MgO and NbN/AlN/MgO films. *Mater. Res. Express* **2015**, *2* (10), 106001.

(4) Volkov, S.; Gregor, M.; Roch, T.; Satrapinskyy, L.; Grančic, B.; Fiantok, T.; Plecenik, A. Superconducting properties of very high quality NbN thin films grown by pulsed laser deposition. *Journal of Electrical Engineering* **2019**, *70* (7), 89−94.

(5) Wang, Z.; Terai, H.; Qiu, W.; Makise, K.; Uzawa, Y.; Kimoto, K.; Nakamura, Y. High-quality epitaxial NbN/AlN/NbN tunnel junctions with a wide range of current density. *Appl. Phys. Lett.* **2013**, *102* (14), 142604.

(6) Nakamura, Y.; Terai, H.; Inomata, K.; Yamamoto, T.; Qiu, W.; Wang, Z. Superconducting qubits consisting of epitaxially grown NbN/AlN/NbN Josephson junctions. *Appl. Phys. Lett.* **2011**, *99* (21), 212502.

(7) Qiu, W.; Makise, K.; Terai, H.; Wang, Z. Developing Superconducting Flux Qubit by Using Epitaxial NbN/AlN/NbN Junction. *Physics Procedia* **2012**, *36*, 360−364.

(8) Kim, S.; Terai, H.; Yamashita, T.; Qiu, W.; Fuse, T.; Yoshihara, F.; Ashhab, S.; Inomata, K.; Semba, K. Enhanced coherence of all-nitride superconducting qubits epitaxially grown on silicon substrate. *Commun. Mater.* **2021**, *2*, 98 DOI: 10.1038/s43246-021-00204-4.

(9) Oliver, W. D.; Welander, P. B. Materials in superconducting quantum bits. *MRS Bull.* **2013**, *38* (10), 816−825.

(10) McDermott, R. Materials Origins of Decoherence in Superconducting Qubits. *IEEE Transactions on Applied Superconductivity* **2009**, *19* (1), 2−13.

(11) Oh, S.; Cicak, K.; Kline, J. S.; Sillanpää, M. A.; Osborn, K. D.; Whittaker, J. D.; Simmonds, R. W.; Pappas, D. P. Elimination of two level fluctuators in superconducting quantum bits by an epitaxial tunnel barrier. *Phys. Rev. B* **2006**, *74* (10), 100502.

(12) Weides, M. P.; Kline, J. S.; Vissers, M. R.; Sandberg, M. O.; Wisbey, D. S.; Johnson, B. R.; Ohki, T. A.; Pappas, D. P. Coherence in a transmon qubit with epitaxial tunnel junctions. *Appl. Phys. Lett.* **2011**, *99* (26), 262502.

(13) Martinis, J. M. Superconducting phase qubits. *Quantum Inf Process* **2009**, *8* (2), 81−103.

(14) Bhat, A.; Meng, X.; Wong, A.; Duzer, T. V. Superconducting NbN films grown using pulsed laser deposition for potential application in internally shunted Josephson junctions. *Supercond. Sci. Technol.* **1999**, *12* (11), 1030−1032.
(15) Roch, T.; Gregor, M.; Volkov, S.; Čaplovičová, M.; Satrapinskyy, L.; Plecenik, A. Substrate dependent epitaxy of superconducting niobium nitride thin films grown by pulsed laser deposition. *Appl. Surf. Sci.* **2021**, *551*, 149333.
(16) Linzen, S.; Ziegler, M.; Astafiev, O. V.; Schmelz, M.; Hubner, U.; Diegel, M.; Il'ichev, E.; Meyer, H.-G. Structural and electrical properties of ultrathin niobium nitride films grown by atomic layer deposition. *Supercond. Sci. Technol.* **2017**, *30* (3), 035010.
(17) Olaya, J. J.; Huerta, L.; Rodil, S. E.; Escamilla, R. Superconducting niobium nitride films deposited by unbalanced magnetron sputtering. *Thin Solid Films* **2008**, *516* (23), 8768−8773.
(18) Talvacchio, J.; Braginski, A. Tunnel junctions fabricated from coherent NbN/MgO/NbN and NbN/Al2O3/NbN structures. *IEEE Trans. Magn.* **1987**, *23* (2), 859−862.
(19) Farha, A. H.; Ufuktepe, Y.; Myneni, G.; Elsayed-Ali, H. E. Pulsed laser deposition of niobium nitride thin films. *AIP Conf. Proc.* **2015**, *1687* (1), 020003.
(20) Kalal, S.; Gupta, M.; Rawat, R. N concentration effects on structure and superconductivity of NbN thin films. *J. Alloys Compd.* **2021**, *851*, 155925.
(21) Johnson, J. P.; Moulton, W. G. Superconducting and normal properties of nbn produced by ion implantation of niobium thin films. *Radiat. Eff. Defects Solids* **1990**, *113* (4), 283−296.
(22) Ermolieff, A.; Girard, M.; Raoul, C.; Bertrand, C.; Duc, T. M. An XPS comparative study on thermal oxide barrier formation on Nb and NbN thin films. *Applications of Surface Science* **1985**, *21* (1), 65−79.
(23) Darlinski, A.; Halbritter, J. Angle-resolved XPS studies of oxides at NbN, NbC, and Nb surfaces. *Surf. Interface Anal.* **1987**, *10* (5), 223−237.
(24) Licata, O. G.; Sarker, J.; Roy, P.; Jia, Q.; Mazumder, B.; Patibandla, N.; Yang, Z.; Wei, X.; Zeng, H.; Zhu, M.; Bachhav, M. Correlation between thickness dependent nanoscale structural chemistry and superconducting properties of ultrathin epitaxial NbN films. *Mater. Chem. Phys.* **2022**, *282*, 125962.
(25) Jouve, G.; Séverac, C.; Cantacuzène, S. XPS study of NbN and (NbTi)N superconducting coatings. *Thin Solid Films* **1996**, *287* (1), 146−153.
(26) Havey, K. S.; Zabinski, J. S.; Walck, S. D. The chemistry, structure, and resulting wear properties of magnetron-sputtered NbN thin films. *Thin Solid Films* **1997**, *303* (1), 238−245.
(27) Isaev, E. I.; Ahuja, R.; Simak, S. I.; Lichtenstein, A. I.; Vekilov, Yu. Kh.; Johansson, B.; Abrikosov, I. A. Anomalously enhanced superconductivity and ab initio lattice dynamics in transition metal carbides and nitrides. *Phys. Rev. B* **2005**, *72* (6), 064515.
(28) Babu, K. R.; Guo, G.-Y. Electron-phonon coupling, superconductivity, and nontrivial band topology in NbN polytypes. *Phys. Rev. B* **2019**, *99* (10), 104508.
(29) Blackburn, S.; Côté, M.; Louie, S. G.; Cohen, M. L. Enhanced electron-phonon coupling near the lattice instability of superconducting NbC1−xNx from density-functional calculations. *Phys. Rev. B* **2011**, *84* (10), 104506.
(30) Gupta, S. D.; Jha, P. K. Smearing induced dynamical stability of NbN and MoN in rocksalt structure. *Physica B: Condensed Matter* **2012**, *407* (12), 1978−1984.
(31) Thompson, K.; Lawrence, D.; Larson, D. J.; Olson, J. D.; Kelly, T. F.; Gorman, B. In situ site-specific specimen preparation for atom probe tomography. *Ultramicroscopy* **2007**, *107* (2), 131−139.
(32) Gault, B.; Moody, M. P.; Cairney, J. M.; Ringer, S. P. Specimen Preparation. In *Atom Probe Microscopy*; Springer, New York, NY, 2012; p 71−110. DOI: 10.1007/978-1-4614-3436-8_4.
(33) Larson, D. J.; Prosa, T. J.; Ulfig, R. M.; Geiser, B. P.; Kelly, T. F. Data Processing and Reconstruction. In *Local Electrode Atom Probe Tomography: A User's Guide*; Springer, New York, NY, 2013; p 109−162. DOI: 10.1007/978-1-4614-8721-0_5.
(34) Gault, B.; Haley, D.; de Geuser, F.; Moody, M. P.; Marquis, E. A.; Larson, D. J.; Geiser, B. P. Advances in the reconstruction of atom probe tomography data. *Ultramicroscopy* **2011**, *111* (6), 448−457.
(35) Kresse, G. Ab initio molecular dynamics for liquid metals. *J. Non-Cryst. Solids* **1995**, *192−193*, 222−229.
(36) Perdew, J. P.; Burke, K.; Ernzerhof, M. Generalized Gradient Approximation Made Simple. *Phys. Rev. Lett.* **1996**, *77* (18), 3865−3868.
(37) Fischer, S.; Karplus, M. Conjugate peak refinement: an algorithm for finding reaction paths and accurate transition states in systems with many degrees of freedom. *Chem. Phys. Lett.* **1992**, *194* (3), 252−261.
(38) Wei, X.; Roy, P.; Yang, Z.; Zhang, D.; He, Z.; Lu, P.; Licata, O.; Wang, H.; Mazumder, B.; Patibandla, N.; Cao, Y.; Zeng, H.; Zhu, M.; Jia, Q. Ultrathin epitaxial NbN superconducting films with high upper critical field grown at low temperature. *Materials Research Letters* **2021**, *9* (8), 336−342.
(39) Villegier, J.-C.; Bouat, S.; Cavalier, P.; Setzu, R.; Espiau de Lamaëstre, R.; Jorel, C.; Odier, P.; Guillet, B.; Mechin, L.; Chauvat, M. P.; Ruterana, P. Epitaxial Growth of Sputtered Ultra-Thin NbN Layers and Junctions on Sapphire. *IEEE Transactions on Applied Superconductivity* **2009**, *19* (3), 3375−3378.
(40) Mazumder, B.; Sarker, J. Probing structural and chemical evolution in (AlxGa1−x)2O3 using atom probe tomography: A review. *J. Mater. Res.* **2021**, *36* (1), 52−69.
(41) Larson, D. J.; Prosa, T. J.; Ulfig, R. M.; Geiser, B. P.; Kelly, T. F. In *Local Electrode Atom Probe Tomography*; Springer, New York, NY, 2013. DOI: 10.1007/978-1-4614-8721-0.
(42) Khan, M. A.; Ringer, S. P.; Zheng, R. Atom Probe Tomography on Semiconductor Devices. *Advanced Materials Interfaces* **2016**, *3* (12), 1500713.
(43) Wang, Z.; Terai, H.; Kawakami, A.; Uzawa, Y. Interface and tunneling barrier heights of NbN/AlN/NbN tunnel junctions. *Appl. Phys. Lett.* **1999**, *75* (5), 701.
(44) Medeiros, O.; Colangelo, M.; Charaev, I.; Berggren, K. K. Measuring thickness in thin NbN films for superconducting devices. *Journal of Vacuum Science & Technology A* **2019**, *37* (4), 041501.
(45) Kalal, S.; Nayak, S.; Tayal, A.; Birch, J.; Rawat, R.; Gupta, M. Microscopic Origin of Structural Disorder in δ-NbN: Correlation of Superconductivity and Electronic Structure. *arXiv* **2020**, 1.
(46) Lisenfeld, J.; Bilmes, A.; Megrant, A.; Barends, R.; Kelly, J.; Klimov, P.; Weiss, G.; Martinis, J. M.; Ustinov, A. V. Electric field spectroscopy of material defects in transmon qubits. *npj Quantum Inf.* **2019**, *5*, 105 DOI: 10.1038/s41534-019-0224-1.
(47) Talvacchio, J.; Sinharoy, S.; Braginski, A. I. Surface stability of NbN single-crystal films. *J. Appl. Phys.* **1987**, *62* (2), 611−614.
(48) Kattel, S.; Atanassov, P.; Kiefer, B. Stability, Electronic and Magnetic Properties of In-Plane Defects in Graphene: A First-Principles Study. *J. Phys. Chem. C* **2012**, *116* (14), 8161−8166.
(49) Albrecht, W.; Kruse, T.; Leo, K.; Kurz, H. Oxygen dependence of the fermi-level and electron-phonon coupling constant in $YBa_2Cu_3O_x$ films. *Appl. Phys. A: Mater. Sci. Process.* **1993**, *56*, 463−465.